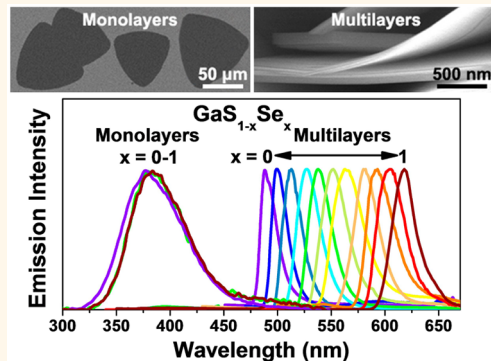


Red-to-Ultraviolet Emission Tuning of Two-Dimensional Gallium Sulfide/Selenide

Chan Su Jung,^{†,‡} Fazel Shojaei,^{‡,§} Kidong Park,[†] Jin Young Oh,[†] Hyung Soon Im,[†] Dong Myung Jang,[†] Jeunghee Park,^{*,†} and Hong Seok Kang^{*,§}

[†]Department of Chemistry, Korea University, Jochiwon 339-700, Korea, [‡]Department of Chemistry and Bioactive Material Sciences and Research Institute of Physics and Chemistry, Jeonbuk National University, Jeonju 560-756, Korea, and [§]Department of Nano and Advanced Materials, College of Engineering, Jeonju University, Jeonju 560-759, Korea. ^{*}C.S.J. and F.S. contributed equally.

ABSTRACT Graphene-like two-dimensional (2D) nanostructures have attracted significant attention because of their unique quantum confinement effect at the 2D limit. Multilayer nanosheets of GaS–GaSe alloy are found to have a band gap (E_g) of 2.0–2.5 eV that linearly tunes the emission in red-to-green. However, the epitaxial growth of monolayers produces a drastic increase in this E_g to 3.3–3.4 eV, which blue-shifts the emission to the UV region. First-principles calculations predict that the E_g of these GaS and GaSe monolayers should be 3.325 and 3.001 eV, respectively. As the number of layers is increased to three, both the direct/indirect E_g decrease significantly; the indirect E_g approaches that of the multilayers. Oxygen adsorption can cause the direct/indirect E_g of GaS to converge, resulting in monolayers with a strong emission. This wide E_g tuning over the visible-to-UV range could provide an insight for the realization of full-colored flexible and transparent light emitters and displays.



KEYWORDS: GaS · GaSe · monolayers · nanosheets · chemical vapor transport · first-principles calculation

The discovery of graphene created the great sensation because of its fascinating properties such as high electron mobility ($2 \times 10^5 \text{ cm}^2 \text{ V}^{-1} \text{ s}^{-1}$ for monolayer) and ballistic conduction that are absent in bulk graphite.^{1,2} However, pristine graphene lacks a band gap, which hampers its application in optoelectronic devices. Researchers have started paying more attention to other graphene-like two-dimensional (2D) materials such as transition metal dichalcogenides (TMDs, *e.g.*, MoS₂, WSe₂) with sizable band gaps as substitutes for, or complements to, graphene.^{3–10} Extensive studies have shown that monolayers of such materials exhibit wider band gaps than their bulk forms, with a stronger photoluminescence (PL) that can be attributed to their direct band gap. An indirect-to-direct band gap transition is the most distinguishing features of 2D TMDs.

Group-III monochalcogenides, such as GaS and GaSe, are particularly (and equally) intriguing layered 2D materials. Previous experimental studies into the band gap of

bulk crystals based on UV-visible absorption, photoluminescence (PL), and photoconductivity have reported an indirect band gap (E_g) of 2.5–2.6 and 2.0–2.1 eV for GaS and GaSe, respectively, with direct band gaps of 3.0–3.1 and 2.12–2.15 eV.^{11–15} Recently, a number of research groups have investigated 2D nanostructures of these materials (including monolayers), showing the fascinating application of optoelectronic devices.^{16–23}

Ab initio calculations predict a *c*-axis confinement-induced blue-shift band gap of the GaS and GaSe monolayers, which is similar to the behavior of TMDs.^{18,21,22,24–28} However, the band gap value depends strongly on the calculation method. For example, PBE functional calculation underestimates the band gap for GaS and GaSe monolayers as 2.5 and 2.1 eV (on average), respectively, and 1.6 and 1 eV for bulk crystals; these values are far less than those obtained experimentally.^{18,21,22,25,27} Rybkovskiy *et al.* have theoretically predicted the band gap of GaSe to be 2.34 eV for the bulk phase and 3.89 eV for a monolayer, with the

* Address correspondence to parkjh@korea.ac.kr, hsk@jj.ac.kr.

Received for review August 5, 2015 and accepted September 5, 2015.

Published online September 05, 2015
10.1021/acsnano.5b04876

© 2015 American Chemical Society

optical absorption of plate-type nanoparticles being presented as evidence for the increased band gap (3.1 eV).²⁴ Ajayan's group have also reported, based on the photocurrent measurement, that the indirect band gap of a GaSe monolayer is 3.3 eV.¹⁹ However, only a small blue shift (20–30 mV) in PL has been observed for few layer-thick GaSe.^{17,29} Furthermore, there is no experimental evidence for a blue-shift in the band gap of GaS. In light of such insufficient data, there is clearly a need to investigate the electronic structures of layered nanostructures using both experimental and theoretical approaches.

In this study, both multilayers and monolayers of $(\text{GaS})_{1-x}(\text{GaSe})_x$ ($\text{GaS}_{1-x}\text{Se}_x$, $0 \leq x \leq 1$) were synthesized by means of chemical vapor transport (CVT). The composition tuning from GaS to GaSe made it possible to more systematically track the nature of electronic structures and band gaps of the GaS–GaSe system. First-principles density-functional theory (DFT) calculations were extensively performed for mono-, bi-, and trilayer structures to support the experimental results. Interest has steadily increased in ternary alloy nanosheets, as these offer an exceptional chance of achieving continuous band gap tuning. Until now, limited success has been reported in synthesizing MoS_2 – MoSe_2 ($E_g = 1.6$ – 1.9 eV), MoS_2 – WS_2 ($E_g = 1.9$ eV), and MoSe_2 – WSe_2 ($E_g = 1.6$ – 1.7 eV) alloy monolayers.^{30–36} $\text{GaS}_{1-x}\text{Se}_x$ alloys examined in their bulk film states showed no restrictions on the concentrations of the components,^{37,38} but there have not yet been any similar studies into nanosheets.

RESULTS AND DISCUSSION

The synthesis and characterization of $\text{GaS}_{1-x}\text{Se}_x$ multilayers and monolayers are described in the Methods. As a first step, a total of 11 multilayer samples were prepared through CVT. The XRD patterns acquired from these samples are shown in Supporting Information Figure S1, and reveal that as x increases the peaks shift from those of GaS to those of GaSe. This is followed by a phase evolution from a pure hexagonal β -GaS phase to a mixture of β - and rhombohedral (R) γ -GaSe phases. The composition (x) was determined based on the peak position of the end members using Vegard's law (*i.e.*, $d = (1 - x)d_{\text{GaS}} + xd_{\text{GaSe}}$), and was found to be consistent with that of scanning electron microscopy energy-dispersive X-ray fluorescence spectroscopy (SEM EDX) data.

The SEM images in Figures 1a,b show the high-density GaS multilayered nanosheets that were grown on large area ($\sim 1 \text{ cm}^2$) substrates. The multilayers with an average thickness of about 20 nm usually fold and aggregate to form a flower-like sheet, probably due to van der Waals force. The same morphology was observed for all other compositions. High-resolution transmission electron microscopy (HRTEM) images of GaS and GaSe nanosheets reveal their single-crystalline nature (Figure 1 panels c, d, and e, respectively).

The insets show corresponding fast Fourier-transform (FFT) images at the [0001] zone axis. Intensity line profiles show that the d spacing between the neighboring (100) planes is 3.1 and 3.25 Å, respectively, which is consistent with the values for β -GaS ($a = 3.587$ Å and $c = 15.492$ Å) and β -GaSe ($a = 3.755$ Å and $c = 15.94$ Å) or γ -GaSe ($a = 3.755$ Å and $c = 23.92$ Å).³⁹ EDX mappings (with scanning transmission electron microscopy (STEM) images) of individual nanosheets show the homogeneous compositional distributions of Ga, S, and Se for $\text{GaS}_{0.9}\text{Se}_{0.1}$, $\text{GaS}_{0.7}\text{Se}_{0.3}$, $\text{GaS}_{0.5}\text{Se}_{0.5}$, $\text{GaS}_{0.3}\text{Se}_{0.7}$, and $\text{Ga}_{0.1}\text{Se}_{0.9}$ (Figure 1f).

Figure 2a displays the UV–visible diffuse reflectance spectrum measured for various compositions of $\text{GaS}_{1-x}\text{Se}_x$ multilayered nanosheets. The formation of a completely miscible solid solution would enable the continuous tuning of the band gaps. We see from this that as x increases, the absorption rises more steeply, which is a characteristic feature of the direct band gap.^{11–15} Based on the Kubelka–Munk (K–M) transformation, the plot of $[F(\nu)h\nu]^{1/2}$ and $[F(\nu)h\nu]^2$ (where $F(\nu)$ is the diffuse reflectance) vs photon energy $h\nu$ (eV) yielded from the linear interpolation the indirect and direct band gaps, respectively (Supporting Information Figure S2). Photoluminescence (PL) spectra were obtained by delivering continuous-wave excitation from a 325 nm He–Cd laser to the as-grown samples at 8 K (Figure 2b). This produced a continuous peak shift during composition tuning without any drastic change in position, intensity, or shape.

The onset of the absorption band, the indirect band gap obtained from the K–M plots, and the PL peak position (at 8 K) all show a linear dependence on the composition, with similar band gap (E_g) values for any given value of x (Figure 2c). The linear fit of this PL data reveals the E_g of GaS and GaSe to be 2.5 and 2.0 eV, respectively; these values are very close to the indirect band gap of the bulk (2.5–2.6 and 2.0–2.1 eV, respectively). Using the K–M plots, the direct band gaps of GaS and GaSe were estimated to be 2.8 and 2.0 eV, respectively. These values are close to the direct band gap of the equivalent bulk phase (3.0–3.1 and 2.12–2.15 eV). The direct band gap decreases linearly to overlap the indirect band gap with increasing x , as shown by the linear fit line. This convergence at $x = 1$ is consistent with that of the bulk film.^{11–15} Therefore, the PL emission is expected to enhance with increasing x , but no significant increase was observed. We discuss this result using the DFT calculations.

Unlike the Au-catalyzed growth of multilayers, the $\text{GaS}_{1-x}\text{Se}_x$ monolayers were grown on SiO_x/Si substrates *via* catalyst-free epitaxy growth. The optical micrographs and photographs in Figure 3a show that the monolayers were homogeneously deposited over a large area of the substrate ($4.5 \times 1.5 \text{ cm}^2$). Note that the color of the substrate is changed from purple (bare) to blue; this occurs for all compositions. In the SEM

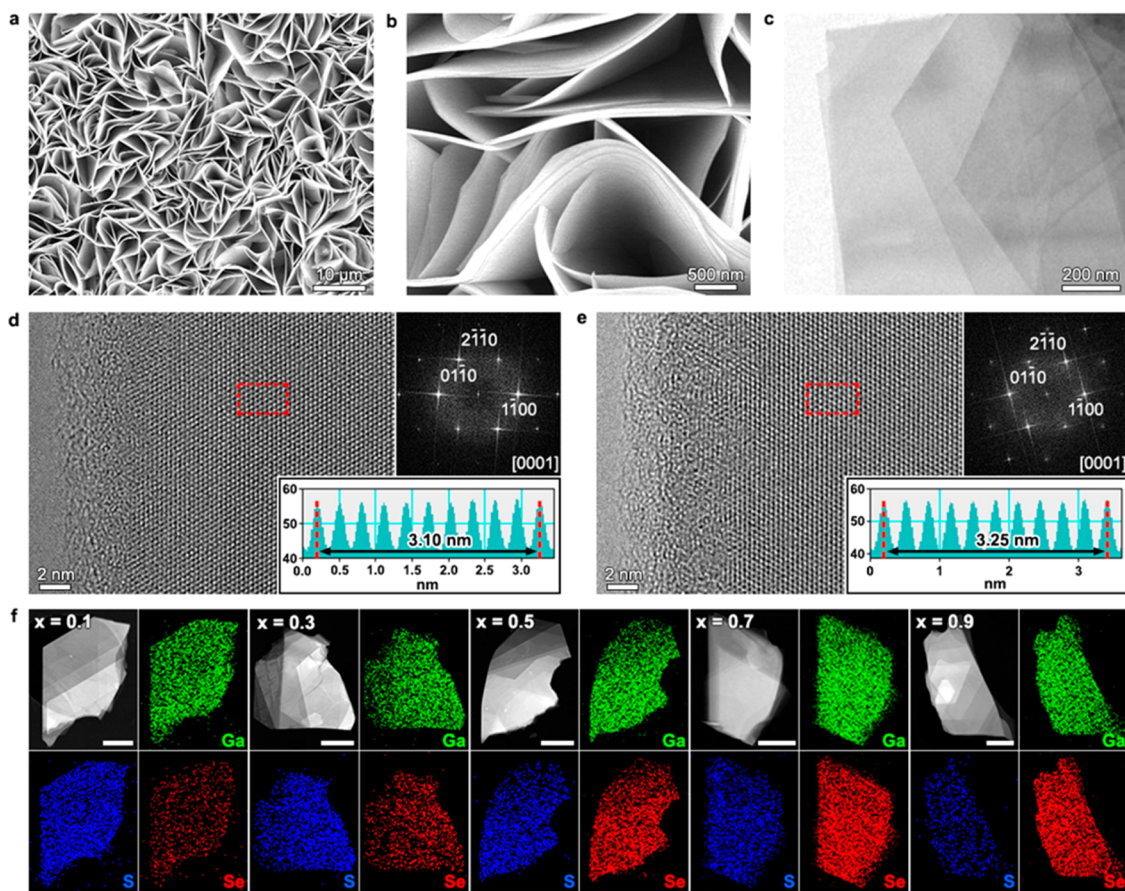


Figure 1. SEM and TEM images of $\text{GaS}_{1-x}\text{Se}_x$ multilayers. (a,b) SEM images of GaS multilayered nanosheets homogeneously grown on a substrate. HRTEM and corresponding FFT images of (c,d) GaS and (e) GaSe multilayers at the zone axis of [0001], showing their single-crystalline nature. The lattice-resolved and FFT images, as well as the intensity line profiles, show that the (100) planes of GaS and GaSe are separated by a distance of 3.1 and 3.25 Å, respectively. (f) EDX mappings (with corresponding STEM image) of individual $\text{GaS}_{1-x}\text{Se}_x$ nanosheets with $x = 0.1, 0.3, 0.5, 0.7$, and 0.9 . Scale bar represents 1 μm .

image of as-grown monolayers (Figure 3b), the triangular shaped monolayers have a lateral dimension of up to 120 μm . The composition of these layers was confirmed by SEM EDX (Supporting Information Figure S3). Atomic force microscopy (AFM) was used to determine the morphology and thickness of the monolayers (Figure 3c); the height profile along the marked line revealing the thickness of the triangular shaped monolayer to be about 0.9 nm. Multilayers are seen to frequently grow at the center of these monolayer triangles, increasing the thickness stepwise by 1.5 and 4.0 nm, containing three and eight layers, respectively. The Raman spectrum was analyzed to confirm the composition tuning of these monolayers, as shown in Supporting Information Figure S4.

The cathodoluminescence (CL, 10 kV) spectrum of the monolayer samples was measured, as shown in Figure 3d. Photographs show the blue-color emission upon the electron beam irradiation (insets). The CL images show the uniformly bright emission of the monolayers; the intensity of GaS is about five times greater than that of GaSe. The CL spectrum (at room temperature) of an individual monolayer consisted of a broad emission band in the range of 300–500 nm

(2.5–4 eV), which peaks at 3.4 and 3.3 eV for GaS and GaSe, respectively. The $\text{GaS}_{0.5}\text{Se}_{0.5}$ monolayers exhibit an emission at 3.3 eV (not shown here), which is similar to that of GaSe. It can therefore be concluded that as the number of layers is reduced to one, the band gap of GaS and GaSe increases by 0.9 and 1.3 eV, respectively, and converges to the nearly same value. It is worth noting here that the CL emission intensity of GaS is enhanced in the monolayers, but decreases by about half in the multilayer region (indicated by arrows). In the case of GaSe, however, the CL emission of the monolayers is approximately three-times weaker than that of the multilayer region (indicated by arrows). This feature was also observed from the $\text{GaS}_{0.5}\text{Se}_{0.5}$ monolayers. The multilayer regions consistently show a red shift in the emission.

As part of this study, we performed DFT calculations for the GaS and GaSe mono-, bi-, and trilayers using the HSE06 and PBE-D2 functionals (see the detailed computation methodology in the Methods). Qiao *et al.* have recently shown that the HSE06 band structures based on the PBE-D2 lattice parameters provide one of the most reliable methods for the calculation of 2D phosphorene,⁴⁰ hence, the same method was employed here to take into account the fact that the

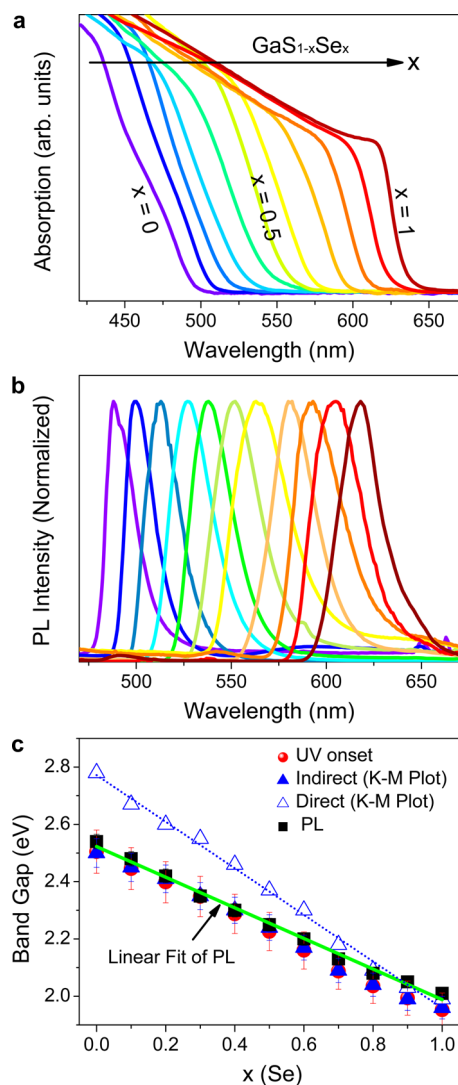


Figure 2. Band gap tuning of $\text{GaS}_{1-x}\text{Se}_x$ multilayers. (a) UV-visible diffuse reflectance spectrum (in absorption) and (b) PL spectrum (at 8 K) of the $\text{GaS}_{1-x}\text{Se}_x$ nanosheets with various values of x . (c) Dependence of the band gap on the Se content (x).

electronic structure is very sensitive to the lattice parameters. It should be emphasized that there has been no systematic comparison of the electronic structures of GaS and GaSe as a function of layer number using this approach. When necessary, the PBE-D2 band structures are also described. Structural parameters, including the lattice constant and the bond length, are shown in Supporting Information Table S1. For trilayer GaSe, its β and γ forms were selected to correlate with the experimental data of the multilayers.

Figure 4 shows the band structures of mono-, bi-, and trilayer structures of GaS and GaSe, obtained from the HSE06 functional calculations. The first diagram illustrates the first Brillouin zone of the hexagonal monolayer structures. All the GaS and GaSe layers exhibit indirect electronic transitions with a valence band maximum (VBM) located between the Γ and K points, as indicated by the red arrow. The direct

electronic transition ($\Gamma \rightarrow \Gamma$) is indicated by the blue arrow. In most cases, there is one more VBM between the Γ and M points that produces a slightly higher energy indirect transition (<0.005 eV). For GaS, conduction band minimum (CBM) is at the M points, while for GaSe it is at the Γ point. When the number of layers increases, the direct and indirect band gaps are simultaneously and significantly diminished due to the strong interlayer interactions along the c axis.

The indirect and direct band gaps with the energy difference between them (ΔE_g) are listed in Table 1. The PBE-D2 band structures were calculated and summarized in Supporting Information Table S2. As usual, the PBE-D2 functional underestimates the band gaps and predicts them 0.6–1 eV smaller than those predicted by the HSE06 functional; these values are less than those obtained experimentally. The HSE06 functional reduces the self-interaction error of the PBE-D2 functional and improves agreement with the experimental data.

Figure 5 panels a and b display the direct/indirect band gap of GaS and GaSe as a function of the layer number for both functional calculations, in which we consistently see a decrease in the band gap of GaS and GaSe as the number of layers increases. The HSE06 functional calculation predicts the indirect band gap of the monolayer to be 3.325 and 3.001 eV for GaS and GaSe, respectively, which is consistent with the experimental data for the monolayers of 3.4 and 3.3 eV. Furthermore, these values agree with those from previous studies using the same functional, thus indicating the accuracy of the methods.^{26,28} For GaS and GaSe trilayers, the indirect band gap decreases to 2.654 and 2.173 (2.199) eV, respectively, which is close to the multilayer values of 2.5 and 2.0 eV. The figure inside parentheses represents the value for the γ phase, while the other value corresponds to the β phase. The direct band gap is 3.133 and 2.181 (2.204) eV for GaS and GaSe, respectively, which is again consistent with the experimental values of the bulk and the multilayers. The β - and γ -GaSe trilayers have similar band structures, which would explain the band gap's linear change with x regardless of the phase mixture.

Additionally, we computed the band gaps for $\text{GaS}_{1-x}\text{Se}_x$ ($x = 0.25, 0.5$, and 0.75) monolayers with various configurations built from a 2×2 cell (see the details in the Supporting Information, Table S3). For the $\text{GaS}_{0.5}\text{Se}_{0.5}$ monolayer, we considered the most stable configurations (A–C) in which S and Se atoms are distributed homogeneously over the two sublayers; (S,Se)–Ga–Ga–(S,Se). They are more stable than the ones having separated S and Se sublayers; S–Ga–Ga–Se. The band gaps (HSE06) are listed in Table 1, showing the similar value for the A–C configurations. The average value is ca. 3.182 and 3.080 eV for direct and indirect band gaps, respectively. The small difference (~0.1 eV) between the direct and indirect band gaps is comparable to that of GaSe. This observation explains the

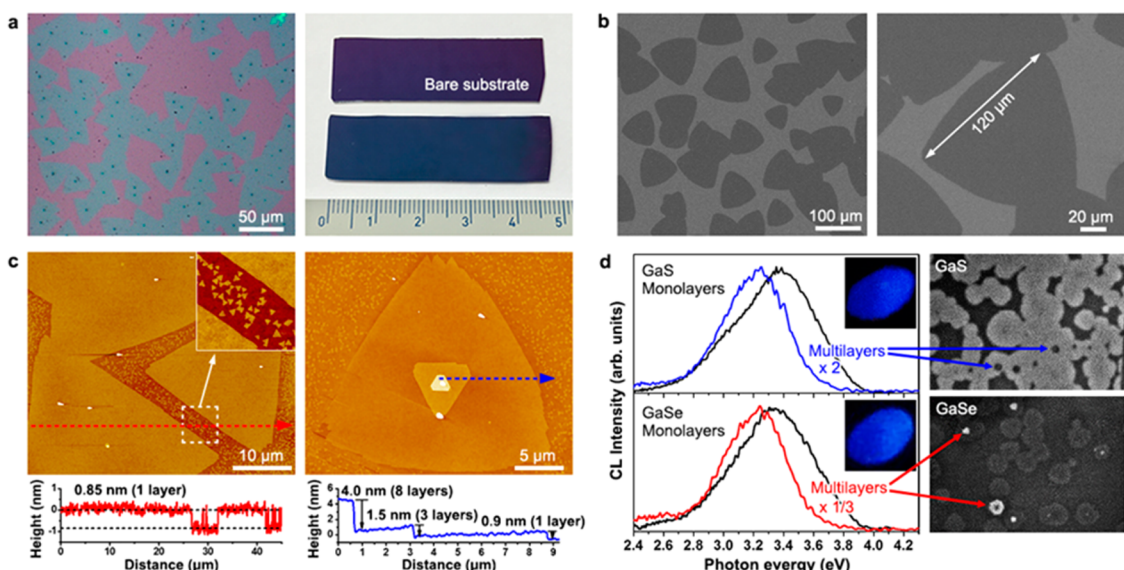


Figure 3. GaS and GaSe monolayers. (a) Optical micrograph and photograph, (b) SEM images, and (c) AFM images of GaSe monolayer samples. Height profiles across the triangle-shaped monolayer and multilayer regions along the lines shown in the AFM images. (d) CL spectrum of the monolayer and multilayer region, with corresponding CL images. Photographs show the blue-color emission of the monolayers (insets).

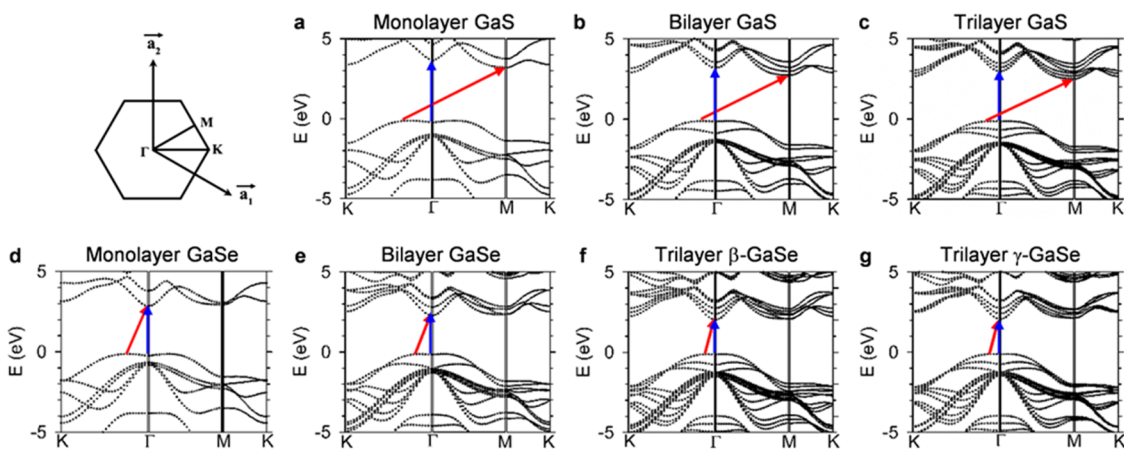


Figure 4. Band structures of GaS and GaSe. First diagram illustrates the first Brillouin zone of the hexagonal monolayer structures. Band structures of (a) mono-, (b) bi-, (c) trilayer β -GaS, (d) mono-, (e) bi-, and (f) trilayer β -GaSe and (g) trilayer γ -GaSe, calculated by the HSE06 functional with the Fermi level set to energy zero. Arrows indicate the indirect (red) and direct (blue) electronic transitions.

reason why the CL properties (including the peak position) of the $\text{GaS}_{0.5}\text{Se}_{0.5}$ monolayer are similar to those of the GaSe monolayer.

The direct band gap of GaS lies above the indirect band gap by a difference of about 0.5 eV (HSE06) or 0.2 eV (PBE-D2). The direct band gap of GaSe is also above the indirect one, but close to each other, the energy difference of less than 0.1 eV (for both HSE06 and PBE-D2) being consistent with that observed in the previous theoretical studies.^{27,28,41} As a consequence, GaS and GaSe are found to exhibit no crossover between their direct and indirect band gaps within the limits of a 2D sheet. This result is quite different from what has been seen in other well-studied TMDs, which exhibit a crossover from indirect-to-direct band gaps in the limit of the monolayer.^{3–10}

In the case of GaSe, the energy difference between the direct and indirect band gaps is so small that electrons can

be thermally distributed in the minima of the CB. The direct band gap transitions are therefore expected to contribute in improving the optical absorption and emission. The CL data for the GaSe monolayer samples show an enhanced emission as the number of layers increases, which can be explained by the fact that the calculated direct and indirect band gaps become closer in value with an increasing number of layers. In contrast, the CL emission of the GaS monolayer sample exhibits the opposite behavior, with its intensity being even larger than that of the GaSe. The present calculations predict that the band gap difference is much larger than that of GaSe, and thus cannot fully explain the strong CL emission of the GaS monolayers.

As noted from previous theoretical works, strain can significantly influence band structures of GaS and GaSe monolayers.^{25–27,42,43} It has also been predicted that the monolayers become a topological insulator under

TABLE 1. Band gaps (E_g) for Optimized Mono-, Bi-, and Trilayer Configurations of GaS and GaSe, Calculated Using HSE06 Functional (All Energies in eV)

no. of Layers	direct ($\Gamma \rightarrow \Gamma$)	indirect	ΔE_g^a	E_{rel}^b
GaS				
1	3.885	3.325 ((K- Γ) \rightarrow M); 3.330 ((Γ -M) \rightarrow M); 3.433 ($\Gamma \rightarrow \Gamma$)	0.560	
2	3.346	2.861 ((K- Γ) \rightarrow M); 2.862 ((Γ -M) \rightarrow M); 2.881 ($\Gamma \rightarrow \Gamma$)	0.485	
3	3.133	2.654 ((K- Γ) \rightarrow M and (Γ -M) \rightarrow M); 2.657 ($\Gamma \rightarrow \Gamma$)	0.479	
GaSe				
1	3.093	3.001 ((K- Γ) \rightarrow Γ); 3.002 ((Γ -M) \rightarrow Γ)	0.092	
2	2.455	2.426 ((K- Γ) \rightarrow Γ); 2.427 ((Γ -M) \rightarrow Γ)	0.029	
3 (β -phase)	2.181	2.173 ((K- Γ) and (Γ -M) \rightarrow Γ)	0.008	
3 (γ -phase)	2.204	2.199 ((K- Γ) and (Γ -M) \rightarrow Γ)	0.005	
$\text{GaS}_{0.5}\text{Se}_{0.5}^c$				
1 (A)	3.150	3.048 ((K- Γ) \rightarrow Γ); 3.053 ((Γ -M) \rightarrow Γ)	0.102	0
1 (B)	3.172	3.071 ((K- Γ) \rightarrow Γ); 3.076 ((Γ -M) \rightarrow Γ)	0.101	0.001
1 (C)	3.224	3.122 ((K- Γ) \rightarrow Γ); 3.127 ((Γ -M) \rightarrow Γ)	0.104	0.001

^a $\Delta E_g = E_g$ (direct) – E_g (indirect); energy difference between the direct and indirect band gaps. ^b Relative energy of configurations per supercell (2 × 2 cell).

^c Three configurations (A, B, and C) were considered.

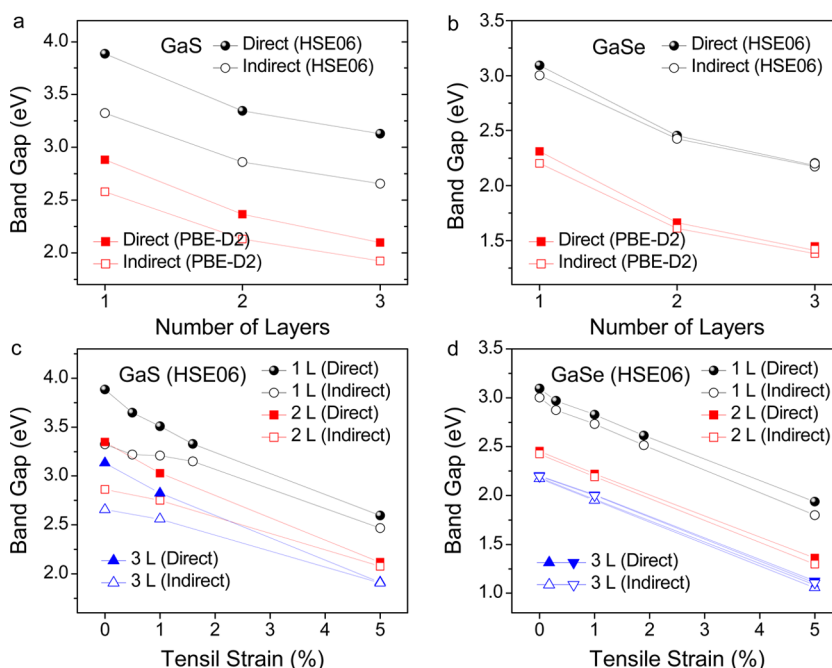


Figure 5. Calculated band gap of mono-, bi-, and trilayers of GaS and GaSe. Band gap of (a) GaS and (b) GaSe as a function of number of layers, as determined using HSE06 and PBE-D2 functional DFT calculations. Band gap (HSE06) of (c) GaS and (d) GaSe mono- (1 L), bi- (2 L), trilayer (3 L) vs biaxial strain (%).

tensile strains. To explore the effects of lattice expansion on the band gap, biaxial tensile strains (up to 7%) were applied to relax the atomic positions at each strain. The band gaps (HSE06 and PBE-D2) obtained from the relaxed configurations are summarized in Supporting Information Table S4. The corresponding band structures are shown in Supporting Information Figure S5 and Figure S6.

Figures 5 panels c and d show the variation of band gaps (HSE06) with biaxial strain (%). The results from the PBE-D2 calculations are shown in Supporting Information Figure S7. At 5% expansion, the HSE06

and PBE-D2 calculated band gap decreases by more than 1 eV. These results are consistent with the behavior of the TMD monolayers.^{44–46} A red shift of PL spectrum was also observed in the mechanically bent multilayer, as shown in Supporting Information Figure S8. The direct band gap of GaSe remains close to the indirect band gap with increasing strain; however, in the case of GaS, the direct and indirect band gaps converge drastically as the strain increases, as was expected from previous calculations of other groups.^{25,42}

In-plane XRD measurements were performed to identify the lattice constants of the monolayers

(see Supporting Information Figure S9). This data show that the lattice constant a is 3.60 and 3.77 Å, for GaS and GaSe monolayers, respectively, which corresponds to an expansion of 0.5% and 0.4% relative to the bulk and the multilayers (3.587 and 3.755 Å, respectively). With 0.5% greater lattice constant, the theoretical direct–indirect band gap difference of the GaS monolayers decreases from 0.560 to 0.427 eV. The unstrained and 0.4% strained GaSe monolayers exhibit nearly the same direct–indirect band gap difference. The strain energy, defined as the total energy difference between the unstrained and strained structures, was calculated to be very small at just 25% that of graphene (see Supporting Information Table S4). We therefore suggest the possibility that the strain can easily narrow the direct–indirect band gap difference of the GaS monolayers, thereby improving their optical transition.

Recent work has reported that O₂ and/or H₂O adsorption on the MoS₂ monolayers influences the performance of field effect transistor devices.^{47,48} Furthermore, adsorption of O₂ molecules enhances the PL emission of *n*-type MoS₂ and MoSe₂ monolayers, while diminishing that of *p*-type WSe₂.^{49,50} Since the GaS and GaSe monolayers are known be *n*- and *p*-type, respectively,^{16,19,20,22,23} there is the possibility that O₂ adsorption may cause the stronger CL emission of GaS monolayers. The effect of O₂ adsorption on the electronic structure of the monolayers in this study was therefore investigated by calculating the adsorption energy (E_{ad}) of $\frac{1}{2}$ an O₂ molecule (*i.e.*, one oxygen atom) onto a 4 × 4 monolayer cell using PBE-D2 functional (see the details in Supporting Information Figure S10). This gave an E_{ad} value of −0.16 eV for a dissociative adsorption that forms S–O–Ga bridge-bonds on the GaS monolayer, but a similar process is less favorable (−0.07 eV) in the case of a GaSe monolayer. We can also expect that chemisorption will be much weaker in the *p*-type GaSe than in the *n*-type GaS.

Analysis of the band structure of the GaS monolayer reveals that oxygen chemisorption induces a convergence of the direct and indirect band gaps, which is caused by a flattening of the VB due to the highly electronegative oxygen atom and Brillouin zone folding. This means that oxygen chemisorption can improve optical transition over a broader energy region. The X-ray photoelectron spectroscopy (XPS) data provides an evidence for the oxygen binding of the monolayers (see Supporting Information Figure S11). Furthermore, the GaS monolayers exhibit a more significant oxygen-binding interaction than the GaSe

monolayers. The oxygen atom can be easily incorporated into the monolayer lattices during epitaxial growth due to the oxide surface of substrates. The calculation also predicts that oxygen chemisorption increases the lattice constant. We therefore propose that the enhanced emission and lattice expansion of the GaS monolayer can be ascribed to an oxygen adsorption. The strong and sharp PL emission of the GaS_{1-x}Se_x multilayers over the entire composition range could be also rationalized by the contribution of the oxygen chemisorption of Ga–S bonding sites. In this sense, it would be informative if the monolayers are subject to the epitaxial growth on the oxygen-free substrates in the future.

CONCLUSIONS

In summary, GaS_{1-x}Se_x multilayers with tunable compositions over the entire range have been successfully synthesized by CVT; the thickness of the multilayers was 20 nm on average. UV–visible absorption and PL data confirmed continuous band gap tuning in the range of 2.0–2.5 eV. Monolayers were also homogeneously synthesized on large area SiO_x/Si substrates, with the measured CL emission revealing GaS_{1-x}Se_x monolayers to exhibit a converged band gap of 3.3–3.4 eV. Interestingly, the CL intensity of the GaS monolayers is prominently enhanced. DFT calculations were performed for mono-, bi-, and trilayer β-GaS and β-GaSe (and γ-GaSe) structures using both HSE06 and PBE-D2 functionals, which found that the direct/indirect band gaps decrease drastically with an increasing number of layers.

The HSE06 calculation identified an indirect band gap for the GaS and GaSe monolayers of 3.325 and 3.001 eV, respectively, which agrees with the experimental values. For trilayer structures, the indirect band gap of GaS, β-GaSe, and γ-GaSe is 2.654, 2.173, and 2.199 eV, respectively, which are both close to the experimental value of the multilayers. The direct band gap of GaS lies about 0.5 eV above the indirect band gap for all layer numbers, whereas the direct and indirect band gaps of GaSe are very close (<0.1 eV). The expansion of the lattice constant a by biaxial tensile strain dramatically reduces the band gaps, and causes the direct band gap in GaS to approach the indirect band gap. It is believed that oxygen adsorption onto GaS monolayers can induce a convergence of the direct and indirect band gaps that may explain their enhanced CL emission. This remarkable visible-to-UV range band gap tuning cannot be achieved with any TMDs, and may allow for development of full-colored atomically thin light-emitting nanodevices.

METHODS

Materials. Ga₂S₃ (99.99%, Sigma-Aldrich) and Ga₂Se₃ (99.99%, Alfa) powders were placed inside a quartz tube reactor. For the growth of multilayered nanosheets, a Si substrate, on which a

1 nm-thick Au film was deposited, was positioned at a distance of 10 cm from the powder source. Argon gas was flowed at a rate of 200 sccm. The temperature of the powder sources was set to 950 °C (for 1 h), and that of the Si substrate was

approximately 700 °C. The composition was controlled using the temperature and the ratio of the two source powders. For a uniform growth of monolayers on large area SiO_x/Si substrates, in which 300 nm-thick SiO_x layers were produced by thermal oxidation, a two-zone furnace was used to control independently the temperatures for the vaporization of the precursors (zone I) and the growth of the monolayer (zone II). The precursors were placed in the upstream zone I, and a substrate was placed at the downstream zone II. After the tube reactor was evacuated to 10 mTorr, zones I and II were heated up to 950 and 700 °C, respectively, and then the growth was conducted at these temperatures for 2–10 min under a pressure of 20 Torr, with an Ar flow (rate = 20 sccm).

Characterization. The structure and composition of the products were analyzed by scanning electron microscopy (SEM, Hitachi S-4700), field-emission transmission electron microscopy (TEM, FEI TECNAI G² 200 kV), high-voltage TEM (HV-TEM, Jeol JEM ARM 1300S, 1.25 MV), and energy-dispersive X-ray fluorescence spectroscopy (EDX). Fast Fourier-transform (FFT) images were generated by the inversion of the TEM images using Digital Micrograph GMS1.4 software (Gatan Inc.). XRD patterns were obtained using a laboratory XRD system (Rigaku, D/MAX-2500 V/PC). In-plane XRD measurement was performed in the 5A beamline of the Pohang Light Source (PLS) with monochromatic radiation. XPS data were obtained using the 8A1 and 8A2 beamlines of the PLS with monochromatic radiation (630 or 680 eV).

UV-visible absorption spectra of the samples were recorded using a spectrometer (Cary 5000, Agilent Tech.). PL (and micro-PL) measurements were performed using a continuous wave (CW) He–Cd laser (λ = 325 nm) or picosecond laser (λ = 355 nm) as the excitation source. The CL spectrum measurements were performed in a SEM (HITACHI S-4300SE) with a Gatan Mono CL3+ system and a liquid nitrogen stage (80–300 K) using an accelerating voltage of 10 keV. The height and topology measurements were carried out using a commercial AFM system (XE-100, Park Systems).

To create the wrinkled nanosheets, elastomeric substrates of PDMS (Sylgard 184, Dow Corning) were prepared by mixing a base resin and curing agent to a ratio of 10:1. Any bubbles present in the unset PDMS were removed in a vacuum chamber, and after curing at 70 °C for 12 h, the resulting polymer film was cut into 40 × 10 mm sized substrates. These flexible PDMS substrates were then stretched by 30–100% using a custom-made strain stage. A contact printing method was applied; nanosheets grown on a Si substrate were rubbed onto a receiver Si substrate under an applied load, and they were then transferred to a prestretched PDMS substrate by applying a tensile force along the nanosheets. Releasing the prestretched substrate induced compressive strains that generated the wrinkles. This prestretched strain is usually defined as ϵ (%) = $\Delta L/L \times 100$, where L is the initial length of the flexible substrate and ΔL is the change in length.

Calculations. The geometric optimization and total energy calculation were done using the Vienna *ab initio* simulation package (VASP).^{51,52} Electron–ion interactions were described by the projector-augmented wave (PAW) method,⁵³ which is essentially a frozen-core all-electron calculation. The van der Waals interaction was estimated through the PBE-D2 calculation, which empirically includes these interactions using Grimme's approach.⁵⁴ Meanwhile, the band structure calculations were done using the Heyd–Scuseria–Ernzerhof (HSE06) hybrid DFT.⁵⁵ Recently, the HSE method, based on an efficient treatment of the nonlocal part of the exchange, was shown to predict impressively accurate band gaps, often similar to those calculated using the GW (the product of the one-body Green function G and the screened Coulomb interaction W) method.

For free-standing GaS and GaSe sheets, our supercell consisted of a 1 × 1 primitive cell. The k -point sampling was done using 29 × 29 × 1 and 19 × 19 × 1 for PBE-D2 and HSE06 methods, respectively. The primitive cell included two Ga atoms and two S (or Se) atoms in two layers. A vacuum of 18 Å along the direction normal to the sheet plane was maintained to allow no appreciable interaction between adjacent cells along the c axis. To investigate the interlayer interaction along the c axis, we adopted the β -form of the crystal—a typical crystal structure in which two 1 × 1 units of the sheet are stacked along the c axis of a supercell in such a way that four Ga and four S atoms are included in the cell, with a stacking sequence of ABAB.

The k -point sampling was done using 29 × 29 × 6 points. For GaSe, we adopted both the β -form and γ -form of the crystals. In the γ -form, six Ga and six Se atoms stack with a sequence of ABCABC. For GaS_{1-x}Se_x (x = 0.25, 0.5, and 0.75) monolayer sheets, the supercell consisted of 2 × 2 cell.

Conflict of Interest: The authors declare no competing financial interest.

Supporting Information Available: The Supporting Information is available free of charge on the ACS Publications website at DOI: 10.1021/acsnano.5b04876.

Table S1–S4, structural parameters, band gaps, realative stabilities; Figure S1–S11, XRD patterns, SEM images, Raman spectra, band structures and band gaps, XPS, configurations (PDF)

Acknowledgment. This study was supported by NRF (20110020090; 2012R1A1A2039084; 2014E1A1A3051259; 2014R1A6A103073; 2009-0082580), and Korea University. The HVEM (Daejeon) and XPS (Pusan) measurements were performed at the KBSI. The experiments at the PLS were partially supported by MOST and POSTECH. We would also like to thank Jeonju University for partial financial support. Computations were performed using a supercomputer of the Korea Institute of Science and Technology Information under Contract No. KSC-2014-C2-001.

REFERENCES AND NOTES

- Novoselov, K. S.; Geim, A. K.; Morozov, S. V.; Jiang, D.; Zhang, Y.; Dubonos, S. V.; Grigorieva, I. V.; Firsov, A. A. Electric Field Effect in Atomically Thin Carbon Films. *Science* **2004**, *306*, 666–669.
- Castro Neto, A. H.; Guinea, F.; Peres, N. M. R.; Novoselov, K. S.; Geim, A. K. The Electronic Properties of Graphene. *Rev. Mod. Phys.* **2009**, *81*, 109–162.
- Neville, R. A.; Evans, B. L. The Band Edge Excitons in 2H-MoS₂. *Phys. Status Solidi B* **1976**, *73*, 597–606.
- Splendiani, A.; Sun, L.; Zhang, Y.; Li, T.; Kim, J.; Chim, C. Y.; Galli, G.; Wang, F. Emerging Photoluminescence in Monolayer MoS₂. *Nano Lett.* **2010**, *10*, 1271–1275.
- Mak, K. F.; Lee, C.; Hone, J.; Shan, J.; Heinz, T. F. Atomically Thin MoS₂: A New Direct-Gap Semiconductor. *Phys. Rev. Lett.* **2010**, *105*, 136805.
- Radisavljevic, B.; Radenovic, A.; Brivio, J.; Giacometti, V.; Kis, A. Single-layer MoS₂ Transistors. *Nat. Nanotechnol.* **2011**, *6*, 147–150.
- Zeng, H.; Dai, J.; Yao, W.; Xiao, D.; Cui, X. Valley Polarization in MoS₂ Monolayers by Optical Pumping. *Nat. Nanotechnol.* **2012**, *7*, 490–493.
- Wang, Q. H.; Kalantar-Zadeh, K.; Kis, A.; Coleman, J. N.; Strano, M. S. Electronics and Optoelectronics of Two-dimensional Transition Metal Dichalcogenides. *Nat. Nanotechnol.* **2012**, *7*, 699–712.
- Jones, A. M.; Yu, H.; Ghimire, N. J.; Wu, S.; Aivazian, G.; Ross, J. S.; Zhao, B.; Yan, J.; Mandrus, D. G.; Xiao, D.; et al. Optical Generation of Excitonic Valley Coherence in Monolayer WSe₂. *Nat. Nanotechnol.* **2013**, *8*, 634–638.
- Zhang, Y.; Chang, T. R.; Zhou, B.; Cui, Y. T.; Yan, H.; Liu, Z.; Schmitt, F.; Lee, J.; Moore, R.; Chen, Y.; et al. Direct Observation of the Transition from Indirect to Direct Bandgap in Atomically Thin Epitaxial MoSe₂. *Nat. Nanotechnol.* **2014**, *9*, 111–115.
- Aulich, E.; Brebner, J. L.; Mooser, E. Indirect Energy Gap in GaSe and GaS. *Phys. Status Solidi B* **1969**, *31*, 129–131.
- Cingolani, A.; Minafra, A.; Tantalo, P.; Paorici, C. Edge Emission in GaSe and GaS. *Phys. Stat. Sol. (a)* **1971**, *4*, K83–K85.
- Mercier, A.; Voitchovsky, J. P. Donor-Acceptor Pair Recombination and Phonon Replica in GaS_xSe_{1-x}. *J. Phys. Chem. Solids* **1975**, *36*, 1411–1417.
- Capozzi, V.; Montagna, M. Optical Spectroscopy of Extrinsic Recombinations in Gallium Selenide. *Phys. Rev. B: Condens. Matter Mater. Phys.* **1989**, *40*, 3182–3190.
- Ho, C. H.; Lin, S. L. Optical Properties of the Interband Transitions of Layered Gallium Sulfide. *J. Appl. Phys.* **2006**, *100*, 083508.

16. Late, D. J.; Liu, B.; Luo, J.; Yan, A.; Matte, H. S. S. R.; Grayson, M.; Rao, C. N. R.; Dravid, V. P. GaS and GaSe Ultrathin Layer Transistors. *Adv. Mater.* **2012**, *24*, 3549–3554.
17. Hu, P. A.; Wen, Z.; Wang, L.; Tan, P.; Xiao, K. Synthesis of Few-Layer GaSe Nanosheets for High Performance Photodetectors. *ACS Nano* **2012**, *6*, 5988–5994.
18. Hu, P. A.; Wang, L.; Yoon, M.; Zhang, J.; Feng, W.; Wang, X.; Wen, Z.; Idrrobo, J. C.; Miyamoto, Y.; Geohegan, D. B.; et al. Highly Responsive Ultrathin GaS Nanosheet Photodetectors on Rigid and Flexible Substrates. *Nano Lett.* **2013**, *13*, 1649–1654.
19. Lei, S.; Ge, L.; Liu, Z.; Najmaei, S.; Shi, G.; You, G.; Lou, J.; Vajtai, R.; Ajayan, P. M. Synthesis and Photoresponse of Large GaSe Atomic Layers. *Nano Lett.* **2013**, *13*, 2777–2781.
20. Zhou, Y.; Nie, Y.; Liu, Y.; Yan, K.; Hong, J.; Jin, C.; Zhou, Y.; Yin, J.; Liu, Z.; Peng, H. Epitaxy and Photoresponse of Two-Dimensional GaSe Crystals on Flexible Transparent Mica Sheets. *ACS Nano* **2014**, *8*, 1485–1490.
21. Yang, S.; Li, Y.; Wang, X.; Huo, N.; Xia, J. B.; Li, S. S.; Li, J. High Performance Few-Layer GaS Photodetector and Its Unique Photo-Response in Different Gas Environments. *Nanoscale* **2014**, *6*, 2582–2587.
22. Li, X.; Lin, M. W.; Puretzky, A. A.; Idrrobo, J. C.; Ma, C.; Chi, M. F.; Yoon, M.; Rouleau, C. M.; Kravchenko, I. I.; Geohegan, D. B.; et al. Controlled Vapor Phase Growth of Single Crystalline, Two-Dimensional GaSe Crystals with High Photoresponse. *Sci. Rep.* **2014**, *4*, 5497.
23. Yuan, X.; Tang, L.; Liu, S.; Wang, P.; Chen, Z.; Zhang, C.; Liu, Y.; Wang, W.; Zou, Y.; Liu, C.; et al. Arrayed van der Waals Vertical Heterostructures Based on 2D GaSe Grown by Molecular Beam Epitaxy. *Nano Lett.* **2015**, *15*, 3571–3577.
24. Rybkovskiy, D. V.; Arutyunyan, N. R.; Orekhov, A. S.; Gromchenko, I. A.; Vorobiev, I. V.; Osadchy, A. V.; Salaev, E. Y.; Baykara, T. K.; Allakhverdiev, K. R.; Obraztsova, E. D. Size-Induced Effects in Gallium Selenide Electronic Structure: The Influence of Interlayer Interactions. *Phys. Rev. B: Condens. Matter Mater. Phys.* **2011**, *84*, 085314.
25. Zhu, Z.; Cheng, Y.; Schwingenschlögl, U. Topological Phase Transition in Layered GaS and GaSe. *Phys. Rev. Lett.* **2012**, *108*, 266805.
26. Zhuang, H. L.; Hennig, R. G. Single-Layer Group-III Monochalcogenide Photocatalysts for Water Splitting. *Chem. Mater.* **2013**, *25*, 3232–3238.
27. Ma, Y.; Dai, Y.; Guo, M.; Yu, L.; Huang, B. Tunable Electronic and Dielectric Behavior of GaS and GaSe Monolayers. *Phys. Chem. Chem. Phys.* **2013**, *15*, 7098–7105.
28. Zólyomi, V.; Drummond, N. D.; Fal'ko, V. I. Band Structure and Optical Transitions in Atomic Layers of Hexagonal Gallium Chalcogenides. *Phys. Rev. B: Condens. Matter Mater. Phys.* **2013**, *87*, 195403.
29. Jie, W.; Chen, X.; Li, D.; Xie, L.; Hui, Y. Y.; Lau, S. P.; Cui, X.; Hao, J. Layer-Dependent Nonlinear Optical Properties and Stability of Non-Centrosymmetric Modification in Few-Layer GaSe Sheets. *Angew. Chem., Int. Ed.* **2015**, *54*, 1185–1189.
30. Gong, Y.; Liu, Z.; Lupini, A. R.; Shi, G.; Lin, J.; Najmaei, S.; Lin, Z.; Elias, A. L.; Berkdemir, A.; You, G.; et al. Band Gap Engineering and Layer-by-Layer Mapping of Selenium-Doped Molybdenum Disulfide. *Nano Lett.* **2014**, *14*, 442–449.
31. Mann, J.; Ma, Q.; Odenthal, P. M.; Isarraraz, M.; Le, D.; Preciado, E.; Barroso, D.; Yamaguchi, K.; von Son Palacio, G.; Nguyen, A.; Tran, T.; et al. 2-Dimensional Transition Metal Dichalcogenides with Tunable Direct Band Gaps: $\text{MoS}_{2(1-x)}\text{Se}_{2x}$ Monolayers. *Adv. Mater.* **2014**, *26*, 1399–1404.
32. Li, H.; Duan, X.; Wu, X.; Zhuang, X.; Zhou, H.; Zhang, Q.; Zhu, X.; Hu, W.; Ren, P.; Guo, P.; et al. Growth of Alloy $\text{MoS}_{2x}\text{Se}_{2(1-x)}$ Nanosheets with Fully Tunable Chemical Compositions and Optical Properties. *J. Am. Chem. Soc.* **2014**, *136*, 3756–3759.
33. Klee, V.; Preciado, E.; Barroso, D.; Nguyen, A. E.; Lee, C.; Erickson, K. J.; Triplett, M.; Davis, B.; Lu, I. H.; Bobek, S.; et al. Superlinear Composition-Dependent Photocurrent in CVD-Grown Monolayer $\text{MoS}_{2(1-x)}\text{Se}_{2x}$ Alloy Devices. *Nano Lett.* **2015**, *15*, 2612–2619.
34. Li, H.; Zhang, Q.; Duan, X.; Wu, X.; Fan, X.; Zhu, X.; Zhuang, X.; Hu, W.; Zhou, H.; Pan, A.; et al. Lateral Growth of Composition Graded Atomic Layer $\text{MoS}_{2(1-x)}\text{Se}_{2x}$ Nanosheets. *J. Am. Chem. Soc.* **2015**, *137*, 5284–5287.
35. Dumcenco, D. O.; Kobayashi, H.; Liu, Z.; Huang, Y. S.; Suenaga, K. Visualization and Quantification of Transition Metal Atomic Mixing in $\text{Mo}_{1-x}\text{W}_x\text{S}_2$ Single layers. *Nat. Commun.* **2013**, *4*, 1351.
36. Zhang, M.; Wu, J.; Zhu, Y.; Dumcenco, D. O.; Hong, J.; Mao, N.; Deng, S.; Chen, Y.; Yang, Y.; Jin, C.; et al. Two-Dimensional Molybdenum Tungsten Diselenide Alloys: Photoluminescence, Raman Scattering, and Electrical Transport. *ACS Nano* **2014**, *8*, 7130–7137.
37. Kuhn, A.; Chevy, A.; Chevalier, R. Interatomic Distances in GaSe_{1-x} . *Phys. Stat. Sol. (a)* **1976**, *36*, 181–187.
38. Terhell, J. C. M.; Brabers, V. A. M.; van Egmond, G. E. Polytype Phase Transition in The Series $\text{GaSe}_{1-x}\text{S}_x$. *J. Solid State Chem.* **1982**, *41*, 97–103.
39. Kuhn, A.; Chevy, A.; Chevalier, R. Crystal Structure and Interatomic Distances in GaSe. *Phys. Stat. Sol. (a)* **1975**, *31*, 469–475.
40. Qiao, J.; Kong, X.; Hu, Z. X.; Yang, F.; Ji, W. High-Mobility Transport Anisotropy and Linear Dichroism in Few-Layer Black Phosphorus. *Nat. Commun.* **2014**, *5*, 4475.
41. Camara, M. O. D.; Mauger, A.; Devos, I. Electronic Structure of the Layer Compounds GaSe and InSe in a Tight-Binding Approach. *Phys. Rev. B: Condens. Matter Mater. Phys.* **2002**, *65*, 125206.
42. Huang, X.; Zhang, X.; Liu, Y.; Wu, Y.; Sa, B.; Ma, M.; Sun, Z.; Liu, R. Different Topological Insulating Behavior in β -GaS and GaS-II under Uniaxial Tension. *Phys. Rev. B: Condens. Matter Mater. Phys.* **2013**, *88*, 235301.
43. An, W.; Wu, F.; Jiang, H.; Tian, G. S.; Li, X. Z. Systematic Investigation on Topological Properties of Layered GaS and GaSe under Strain. *J. Chem. Phys.* **2014**, *141*, 084701.
44. Feng, J.; Qian, X.; Huang, C. W.; Li, J. Strain-Engineered Artificial Atom as a Broad-Spectrum Solar Energy Funnel. *Nat. Photonics* **2012**, *6*, 866–872.
45. Johari, P.; Shenoy, V. B. Tuning the Electronic Properties of Semiconducting Transition Metal Dichalcogenides by Applying Mechanical Strains. *ACS Nano* **2012**, *6*, 5449–5456.
46. Shi, H.; Pan, H.; Zhang, Y. W.; Yakobson, B. I. Quasiparticle Band Structures and Optical Properties of Strained Monolayer MoS_2 and WS_2 . *Phys. Rev. B: Condens. Matter Mater. Phys.* **2013**, *87*, 155304.
47. Tongay, S.; Zhou, J.; Ataca, C.; Liu, J.; Kang, J. S.; Matthews, T. S.; You, L.; Li, J.; Grossman, J. C.; Wu, J. Broad-Range Modulation of Light Emission in Two-Dimensional Semiconductors by Molecular Physisorption Gating. *Nano Lett.* **2013**, *13*, 2831–2836.
48. Nan, H.; Wang, Z.; Wang, W.; Liang, Z.; Lu, Y.; Chen, Q.; He, D.; Tan, P.; Miao, F.; Wang, X.; et al. Strong Photoluminescence Enhancement of MoS_2 through Defect Engineering and Oxygen Bonding. *ACS Nano* **2014**, *8*, 5738–5745.
49. Late, D. J.; Liu, B.; Matte, H. S. S. R.; Dravid, V. P.; Rao, C. N. R. Hysteresis in Single-Layer MoS_2 Field Effect Transistors. *ACS Nano* **2012**, *6*, 5635–5641.
50. Cho, K.; Park, W.; Park, J.; Jeong, H.; Jang, J.; Kim, T. Y.; Hong, W. K.; Hong, S.; Lee, T. Electric Stress-Induced Threshold Voltage Instability of Multilayer MoS_2 Field Effect Transistors. *ACS Nano* **2013**, *7*, 7751–7758.
51. Kresse, G.; Hafner, J. Ab initio Molecular Dynamics for Liquid Metals. *Phys. Rev. B: Condens. Matter Mater. Phys.* **1993**, *47*, 558–561.
52. Kresse, G.; Furthmüller, J. Efficient Iterative Schemes for ab initio Total-Energy Calculations Using a Plane-Wave Basis Set. *Phys. Rev. B: Condens. Matter Mater. Phys.* **1996**, *54*, 11169–11186.
53. Kresse, G.; Joubert, D. From Ultrasoft Pseudopotentials to the Projector Augmented-Wave Method. *Phys. Rev. B: Condens. Matter Mater. Phys.* **1999**, *59*, 1758–1775.
54. Grimme, S. Semiempirical GGA-Type Density Functional Constructed with a Long-Range Dispersion Correction. *J. Comput. Chem.* **2006**, *27*, 1787–1799.
55. Heyd, J.; Scuseria, G. E.; Ernzerhof, M. Hybrid Functionals Based on a Screened Coulomb Potential. *J. Chem. Phys.* **2003**, *118*, 8207–8215.